PIER

Optimization Design of Photonic-Crystal Surface-Emitting Lasers: Toward Large Bandwidth and Single-Lane 200 G Optical Transmission

Xing-Chen Ai[1, 2], Shao-Chi Pan[3], Yu-Hao Wang[1, 2], and Si-Cong Tian[1, *]

[1]*Bimberg Chinese-German Center for Green Photonics & Key Laboratory of Luminescence Science and Technology*
Chinese Academy of Sciences & State Key Laboratory of Luminescence and Applications
Changchun Institute of Optics, Fine Mechanics and Physics
Chinese Academy of Sciences, Changchun 130033, China
[2]*University of Chinese Academy of Sciences, Beijing 100049, China*
[3]*College of Integrated Circuits and Optoelectronic Chips*
Shenzhen Technology University, Shenzhen 518118, China

ABSTRACT: By using the time-dependent three-dimensional coupled-wave theory (3D-CWT), the transient analysis of photonic-crystal surface-emitting lasers (PCSELs) with double-lattice photonic crystals is performed. By optimizing the size of the PCSELs and the shape of the double-lattice photonic crystals, the resonance frequency is increased, and the damping (photon lifetime) is decreased, which enables over 40 GHz intrinsic 3 dB modulation bandwidth of the PCSELs. 100 Gb/s open eye under non-return-to-zero (NRZ) modulation is demonstrated by using such PCSELs. The large bandwidth enables single-lane 200 G optical transmission under four-level pulse-amplitude modulation (PAM-4). This study shows the design principles of large-bandwidth PCSELs and promises PCSELs to be an ideal candidate for the application of high-speed, high-power, free-space optical communication.

1. INTRODUCTION

Semiconductor lasers, such as vertical-cavity surface-emitting lasers (VCSELs), and distributed feedback (DFB) lasers are essential for high-speed optical transmission. Surface-emitting lasers, for example, VCSEL, have the advantages of near-circular far-field pattern, convenient testing, compact structure, low cost, etc. Currently, the 3 dB bandwidth of directly modulated VCSELs exceeds 33 GHz for 850 nm [1], 35 GHz for 980 nm [2], and 29 GHz for 1060 nm VCSEL [3]. Single-channel non-return-to-zero (NRZ) transmission rates are increased to 106.25 Gb/s for 850 nm VCSEL [1, 4] and 128 Gb/s for 1060 nm VCSEL [5]. Single-channel four-level pulse-amplitude modulation (PAM-4) transmission rates based on 850 nm and 1060 nm VCSELs surpass 100 Gb/s [1, 5]. More than 200 Gb/s PAM-4 transmissions for 850 nm VCSELs over 100 Gb/s for 940 nm, and 144 Gb/s PAM-4 transmissions for 1060 nm VCSELs based on advanced electronic technologies have been verified [5–7]. However, the output power of high-speed VCSELs is limited to the milliwatt level, which limits their application requirements.

Photonic-crystal surface-emitting lasers (PCSELs) have a transverse resonator, and the light emits from the surface. PC-SELs offer advantages of high power, single-mode, and narrow linewidth [8, 9]. The highest single-mode power in the continuous-wave output reached 50 W [10], and the prediction for the power of 500 W–1 kW was proposed [11]. Nevertheless,

research has been expanded into 1.3 μm [12] and 1.5 μm [13] long-wavelength PCSELs, as well as electrical-injection terahertz (THz) PCSEL [14], high-brightness PCSELs [15], and ultrafast photonics of PCSEL [16].

Due to the advantages of PCSELs, PCSELs present opportunities for high-speed long-distance fiber optical communication and free-space optical (FSO) transmission [17, 18], and have the potential to enhance the performance of space communication systems, including space-to-ground links, deep-space links, and inter-satellite links [19]. Previous studies have conducted frequency response and bandwidth measurements of PCSELs [20–22]. The results show that the bandwidth of PC-SELs exceeds 4 GHz. The experiment of FSO transmission based on PCSEL with the rates of 480 MHz and 864 MHz has been verified [17]. The bandwidth of watt-class PCSEL with the size of 500 μm × 500 μm watt-class PCSEL is increased to several GHz levels, and the transmission rate of 10 Gbit/s with the distance of 5 km is achieved [18]. A comprehensive analysis of the time-dependent three-dimensional coupled-wave theory of PCSEL is given [23], which provides a methodology for analyzing the high-speed performance. The simulation of PC-SEL with the design of ellipse double lattice photonic crystal holes and the device size of 300 μm × 300 μm is conducted. On the other hand, mode control is a significant issue for PC-SELs [13, 24, 25]. To confine the mode distribution and optical field, previous studies have employed various approaches such as reflective surfaces at the boundary of the resonant sur-

---

face [26], external reflection outside the photonic-crystal region and inside the device [27], one-dimensional gratings [28], or photonic crystals confined by energy band [13]. These state-of-the-art structures serve as powerful methods for achieving high-speed modulation when reducing the size of devices.

However, in the above studies, the sizes of the PCSELs are no less than 200 μm, or additional structures are introduced, to keep enough lateral optical confinement and lasing. In addition, none of the works have considered how to tune the photon lifetime and the damping to increase the 3 dB modulation bandwidth of the PCSELs. Therefore, in this paper, we use double-lattice photonic crystals to reduce the size of the PCSEL to 100 μm to improve the high-speed performance. The smaller size leads to a larger D factor and a larger resonance frequency of the PCSELs. We also tune the distance between the double lattice and the diameters of the double lattice to increase the in-plane loss. The increased in-plane loss leads to a smaller photon lifetime and damping. The larger resonance frequency and smaller damping together result in a larger 3 dB modulation bandwidth. The structure of the paper is as follows: in Section 2, we introduce the design principle for high-speed PCSELs and our design of PCSELs. In Section 3, we calculate the output power, modes, and small signal response of the PCSELs by the three-dimensional coupled-wave theory (3D-CWT) method [23] and show the eye diagram by using such PCSELs. We realize over 40 GHz intrinsic 3 dB modulation bandwidth of the PCSELs and over 100 Gbit/s single-lane optical transmission under NRZ modulation. The last is the summary.

2. FINITE-SIZE COUPLED-WAVE THEORY

Calculation tools for PCSELs include the Plane Wave Expansion Method (PWEM), Rigorous Coupled-Wave Analysis (RCWA), and Finite-Difference Time-Domain (FDTD). PWEM and RCWA face challenges when being applied to finite-sized structures, while FDTD simulations of large devices demand extensive computational resources. 3D coupled-wave equations that consider vertical field distribution, making it applicable to a variety of PC structures, double circular [13], double elliptical [15], double elliptical-circular [17], triangular [29] lattices, etc. This method effectively highlights the coupling effects among vectors in three-dimensional space. 3D coupled-wave equations for finite sizes are described as [30]

$$(\delta + i\alpha) \begin{pmatrix} R_x \\ S_x \\ R_y \\ S_y \end{pmatrix} = C \begin{pmatrix} R_x \\ S_x \\ R_y \\ S_y \end{pmatrix} + i \begin{pmatrix} \frac{\partial R_x}{\partial x} \\ -\frac{\partial S_x}{\partial x} \\ \frac{\partial R_y}{\partial y} \\ -\frac{\partial S_y}{\partial y} \end{pmatrix}, \quad (1)$$

where R_x, S_x, R_y, and S_y are amplitudes of basic waves in the direction of $\pm x$ and $\pm y$; δ is the deviation from the Bragg condition; α is the modal loss; C is the 4×4 matrix and is the sum of C_{1D}, C_{2D}, and C_{rad}, corresponding to the coupling of basic, high orders, and radiative waves. The modal loss α is calculated by solving the equations using the finite differential

method [29] and is affected by the finite device size L^2. The modal loss α is calculated by solving the equations using the finite differential method [29] and is affected by the finite device size L^2. α is the sum of the vertical loss $\alpha_\perp$ that is perpendicular to the photonic-crystal resonance surface and the in-plane loss of the surface $\alpha_{//}$ that is the vertical part of modal loss. α can also be given by the following expressions [30]:

$$\alpha = \alpha_\perp + \alpha_{//}. \quad (2)$$

The vertical loss and in-plane loss are calculated by the ratio of vertical direction power P_{rad} to the in-plane power escaping from edges P_{edge} [30]:

$$P_{stim} = P_{rad} + P_{edge}, \quad \alpha_\perp = \alpha \frac{P_{rad}}{P_{stim}}, \quad \alpha_{//} = \alpha \frac{P_{edge}}{P_{stim}}, \quad (3)$$

Based on the above calculations, the losses of the lasing modes can be determined and converted into photon lifetime. In the next section, the photon lifetime will be optimized to decrease the damping, in turn, increase the bandwidth, and bite rate.

Rate equations describing carrier-photon interactions are linked with coupled-wave equations in time-dependent equations. Because of this, the gain can be calculated from the spatial carrier distribution, which is then incorporated into the coupled-wave equation to determine the field distribution. Since the photon number at a given spatial point can be described by the field amplitude, R_x, S_x, R_y, and S_y, the photon number can be calculated and subsequently introduced into the rate equations, thereby giving feedback to the carrier distribution. The time-dependent coupled-wave equation is expressed as follows [23]:

$$\frac{\partial}{\partial t} \begin{pmatrix} R_x \\ S_x \\ R_y \\ S_y \end{pmatrix} = \frac{c}{n_g} \left(-i\delta + \frac{g - \alpha_{in}}{2} \right) \begin{pmatrix} R_x \\ S_x \\ R_y \\ S_y \end{pmatrix}$$

$$- \frac{c}{n_g} \begin{pmatrix} \partial R_x/\partial x \\ -\partial S_x/\partial x \\ \partial R_y/\partial y \\ -\partial S_y/\partial y \end{pmatrix} - \gamma_{ind} \begin{pmatrix} R_x \\ S_x \\ R_y \\ S_y \end{pmatrix}$$

$$+ \frac{c}{n_g} C \begin{pmatrix} R_x \\ S_x \\ R_y \\ S_y \end{pmatrix} + \begin{pmatrix} f_1 \\ f_2 \\ f_3 \\ f_4 \end{pmatrix}, \quad (4)$$

where n_g is the group index; g is the gain related to carrier density; α_{in} is the internal material loss; γ_{ind} is the rate of index changing and is neglected; f_1, f_2, f_3, and f_4 are the noise related to spontaneous emission. The rate equation associated with carriers is expressed as follows [23]:

$$\frac{\partial N}{\partial t} = \frac{J}{ed_{active}} - \frac{N}{\tau_c} - \frac{c}{n_g} gN + D_0 \nabla^2 N, \quad (5)$$

TABLE 1. Parameters for simulations.

Parameter	Symbol	Value	Source
Period of photonic cells (constant lattice)	T	277 nm	From Ref. [23]
Maximum Gain	$g_{\max}$	2000 cm^{-1}	From Ref. [23]
Absorption Coefficient	g_0	-5000 cm^{-1}	From Ref. [23]
Transparency Carrier Density	N_{tr}	1.5×10^{18} cm^{-3}	From Ref. [23]
Current Spread outside the Electrode	σ_r	25 μm	From Ref. [23]
Carrier Lifetime	τ_c	1.5 ns	From Ref. [23]
Diffusion Constant of Carrier	D_0	100 cm^2/s	Typical value; From Ref. [23]
Spontaneous Emission Factor	β	1×10^4	Typical value; also used in Ref. [23]
Internal Loss of Materials	α_{in}	5 cm^{-1}	Typical value; From Ref. [23]
Optical Confinement Factor (in Active Layer)	Γ_{active}	0.066	Calculated by the transfer matrix method
Optical Confinement Factor (in PC Layer)	Γ_{PC}	0.2273	Calculated by the transfer matrix method
Group Refractive Index	n_g	3.485	Calculated by the transfer matrix method
Effective refractive index	n_{eff}	3.3832	Calculated by the transfer matrix method

where the photon density U is [23]:

$$U = \frac{2\varepsilon_0 n_{eff} n_g \Gamma_{active}}{\hbar \omega d_{active}} \left(|R_x|^2 + |S_x|^2 + |R_y|^2 + |S_y|^2 \right), \quad (6)$$

here, N is the carrier density, d_{active} the active layer thickness, τ_c the carrier lifetime, D_0 the diffusion coefficient of the carriers, Γ_{active} the optical confinement factor in active layers, ε_0 vacuum dielectric constant, and n_{eff} the effective index. The following simulation of dynamic characteristics is performed based on the numerical solution of the equations.

3. PCSEL DESIGN

3.1. The Structure and the Lattice Type of the PCSELs

The structure of double-lattice is favorable for suppressing higher order feedback and is much more possible to achieve single-mode operation [31]. A larger area corresponds to lower in-plane loss, which will be verified in the calculation in Section 3.3. For the device with a large area and elliptical double-lattices as reported in [15], a one-dimensional coefficient is reduced, and a two-dimensional coefficient is maintained to let field distributions be flat and lights "spread" in the resonator [15]. However, it can be inferred that for smaller area devices aiming to achieve high-speed operation with higher in-plane loss and weak capability to confine the optical field, the field distribution should be concentrated as much as possible.

To obtain a more rigorous and subsequent high-speed characteristics analysis, the simulated material structure (Figure 1) designed for 940 nm in [23], which proposes the time-dependent coupled-wave model, is used. By giving an average index of the photonic-crystal layer n_{ave}, the corresponding longitudinal
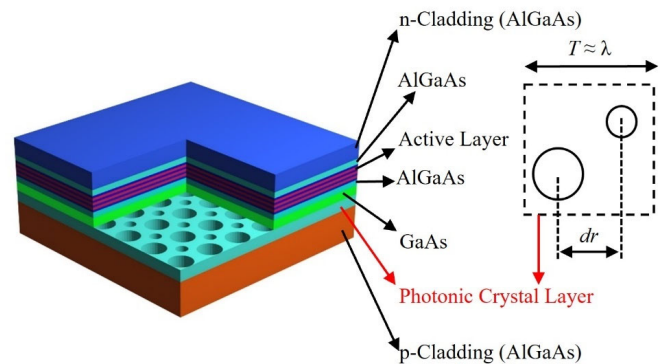

FIGURE 1. Schematic cross-section of the PCSEL. T is the lattice constant and dr is the horizontal distance between two holes.

electric field distribution is calculated and plotted in Figure 2. Parameters for calculations and part of the different parameters attributed to different selected n_{ave} are listed in Table 1. It can be observed that the photonic crystal layer, after "etching" the photonic-crystal lattice, exhibits a lower refractive index which enhances field confinement. This results in a narrower-waist field distribution with the peak shifted closer to the active layer. To further strengthen confinement and increase both the optical confinement factor in the active layer and the photonic-crystal layer, we set the average refractive index of the photonic-crystal layer to be close to that of the p-cladding layer. Based on the proposed "epitaxial" structure, the methodology of design of a high-speed 940 nm PCSEL by optimization of the relaxation oscillation frequency and damping will be proposed in this section.

The measurement results show a 3 dB bandwidth of 4 GHz in [18]. In this paper, the optimized results suggest that the
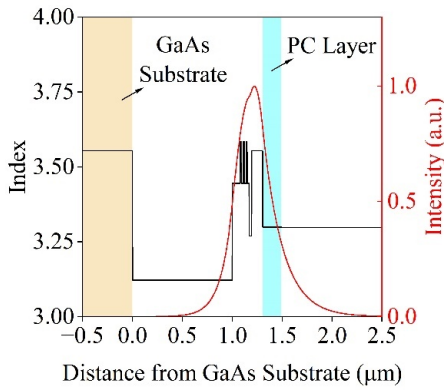
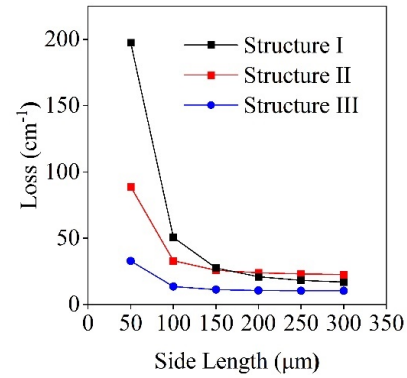**FIGURE 2.** The index and longitudinal field distribution of the PCSEL.

FIGURE 3. The overall loss of the three PCSELs as the function of the side length. The loss increases exponentially as the size decreases.

3 dB bandwidth can be further enhanced through the methods introduced above, which are summarized as follows: (1) reducing device sizes to increase the D-factor and the resonant frequency (f_r), (2) optimizing the design of the double-lattice photonic-crystal to decrease the photon lifetime and optimize the damping.

Unlike realizing larger output power of PCSELs, this work is based on material layers in [23] and aims to further enhance the 3 dB bandwidth of the PCSEL. A key requirement is to increase the optical confinement factor to increase D-factor and the resonance frequency. A larger optical confinement factor can be achieved by tuning of n_{ave}, which can be realized by increasing the total fill-factor of the photonic-crystal layer. In our design, the optical confinement factor is 0.066, which is slightly smaller than previously reported value of 0.085 in [13] and larger than the value of 0.044 in [23] and 0.4 in [18]. The confinement factor of the typical VCSEL is ~ 0.038 [32]. Therefore, a larger optical confinement factor of the PCSEL is beneficial to realizing an equal or larger 3 dB bandwidth compared to that of the VCSEL.

3.2. Design Principles for High-Speed PCSELs

The intrinsic transfer function of lasers from general rate functions is expressed as [32–34]:

$$H(f) = C_0 \cdot \frac{f_r^2}{f_r^2 - f^2 + i \frac{f}{2\pi}\gamma}, \quad (7)$$

where

$$f_r = D\sqrt{I - I_{th}}, \quad D = \frac{1}{2\pi}\sqrt{\frac{\eta_i \Gamma_{active} v_g a_N}{q V_a \chi}}, \quad (8)$$

$$\gamma \approx K f_r^2 + \gamma_0, \quad K = 4\pi^2 \left(\tau_p + \frac{\varepsilon \chi}{v_g a_N} \right), \quad (9)$$

$$\gamma_0 \approx \frac{1}{\tau_{\Delta N}} + \frac{\Gamma_{active} R'_{sp}}{N_p},$$

where C_0 is a constant, f_r the relaxation frequency, D the D-factor, γ the damping, I_{th} the threshold current, η_i the internal

efficiency, v_g the group velocity, a_N the differential gain, V_a the volume of active layers, τ_p the photon lifetime, χ the transport factor, ε the gain compression factor related to nonlinear gain effects, γ_0 the bias of damping caused by carrier lifetime, $\tau_{\Delta N}$ the differential carrier lifetime, R'_{sp} the spontaneous emission rate, and N_p the photon density. A large f_r and a small γ are beneficial to a large 3 dB modulation bandwidth [34]. f_r is determined by the D-factor and the current above the threshold, and γ varies with the K-factor, which is approximately linearly related to τ_p. According to formula (8), to achieve a larger f_r, it needs to reduce the V_a but increase Γ_{active} and increase the injection current above the threshold current. A larger D-factor enables a larger f_r at lower bias currents. Therefore, reducing the device size is necessary.

Besides, the loss (photon lifetime) can be modified by tuning the area fill factor and relative distance between two photonic-crystal holes "dr". The optimized method is that by increasing the loss, photon lifetime and damping decrease, and it is possible to obtain a larger 3 dB modulation bandwidth as referenced from [35–37]. However, it should be noted that the loss cannot always help the 3 dB modulation bandwidth to increase for high-speed lasers [35].

3.3. Numerical Results

Here, we optimize the photonic-crystal structure to have a large relaxation frequency and a small damping. The relationship between loss and size of the PCSEL with the same photonic crystal cell is calculated and shown in Figure 3, to analyze the impact of the size of the PCSEL. For the same photonic-crystal structure, the loss increases exponentially as the device size decreases. Although a smaller size helps large relaxation oscillation frequency, it leads to increased leakage of optical energy, complicating the achievement of stable optical modes and lasing. Due to the significant exponential increase in loss when the size is smaller than 100 μm and the corresponding decrease in vertical loss ratio, the simulation dimensions are determined to be 100 μm × 100 μm.

Figure 4(a) presents the total loss, defined as the sum of vertical radiation loss and edge loss [30], under varying relative fill factors and the distance between the two holes in one crystal
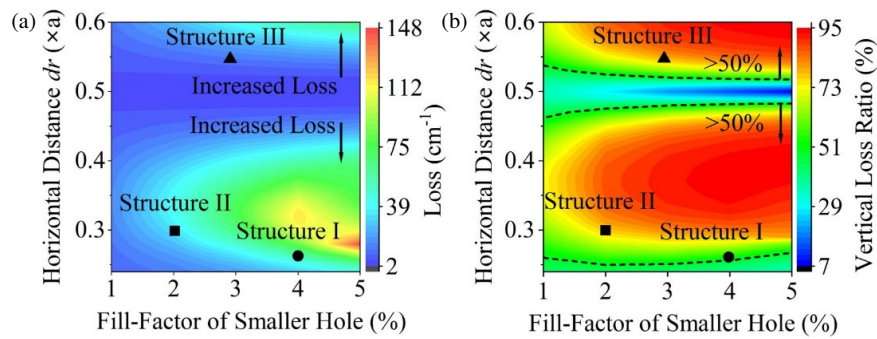
FIGURE 4. (a) The total loss (the sum of vertical radiation loss and edge loss) under different fill factors and horizontal distances between two holes. The optimal total loss is concentrated within a banded region, which lies between the areas of excessive high and low losses. (b) The vertical loss (surface emission loss) ratio under different fill factors and horizontal distances between two holes. The vertical loss is dominant if the ratio is larger than 50%. The circular, square, and triangular symbols correspond to structures I, II, and III.

TABLE 2. Parameters of different structures of circular double-lattice.

Structure of Double-Lattice	I	II	III
Side Length of PC	100 µm		
Side Length of PC-Lattice	277 nm		
Structure Pattern			
Lowest Loss	50.09 cm^{-1}	33.96 cm^{-1}	13.46 cm^{-1}
Photon Lifetime	2.32 ps	3.42 ps	8.63 ps
Vertical Loss Ratio	51.61 %	70.06 %	80.62 %

lattice. Excessive large in-plane loss leads to more leakage at the edge of the plane, and it is not suitable for the confinement of the optical field, while excessive small loss makes it difficult to conduct high-speed operation. The optimal total loss is concentrated within a band region, positioned between the regions of excessively large and small losses. Figure 4(b) illustrates the vertical loss (surface emission loss) ratio for different relative fill factors and the distance between the two holes in one crystal lattice. Since vertical loss represents the output lasing, a larger value is desired to enhance output power. The vertical loss becomes the dominant loss when its ratio exceeds 50%. However, the mode selection is governed by edge loss when edge loss dominates [30]. Therefore, we select three kinds of circular double-lattice structures with different losses, that can be converted to the photon lifetime. The vertical loss ratio of all three structures exceeds 50%. Parameters of different structures of circular double-lattice are shown in Table 2.

The mode with the lowest loss is referred to as "mode A", the next lowest loss mode excluding numerical artifacts [26] as is referred to "mode B". "mode C", and "mode D" are located at the bands with shorter wavelengths.

Figures 5(a), (e), and (i) illustrate the wavelengths corresponding to the losses of various modes calculated by solving the coupled-wave equations for PCSELs with 100 µm side

length. The lowest losses of the three devices are 50.09 cm^{-1}, 33.96 cm^{-1}, and 13.46 cm^{-1}, respectively, and the corresponding photon lifetimes are 2.32 ps, 3.42 ps, and 8.63 ps, respectively. The total loss shows the threshold gain, where a shorter photon lifetime corresponds to a larger threshold gain. The mode with the lowest loss is referred to as "mode A" and the next lowest loss mode excluding numerical artifacts [26] as referred to "mode B". "mode C" and "mode D" are located at the bands with shorter wavelengths. As the minimum loss decreases, the bandgap expands, causing mode A to redshift away from the central wavelength, and the loss difference between mode A and mode C increases. Mode A has the lowest loss and becomes the lasing mode, while mode C is called leaky mode [30] which makes it hard to establish a stable photon density distribution. Second higher-order mode B is often located at a shorter wavelength. Calculated photonic-crystal band diagrams for structure I, II, and III are shown in Figures 5(b), (f), and (j). In addition, for lasing modes, field intensities are shown in Figures 5(c), (g), (k), and far-field (FF) patterns are shown in Figures 5(d), (h), (l). The field intensity distribution and FF pattern of the lasing mode exhibits a single lobe, in contrast to the multiple lobes typically associated with higher-order modes.
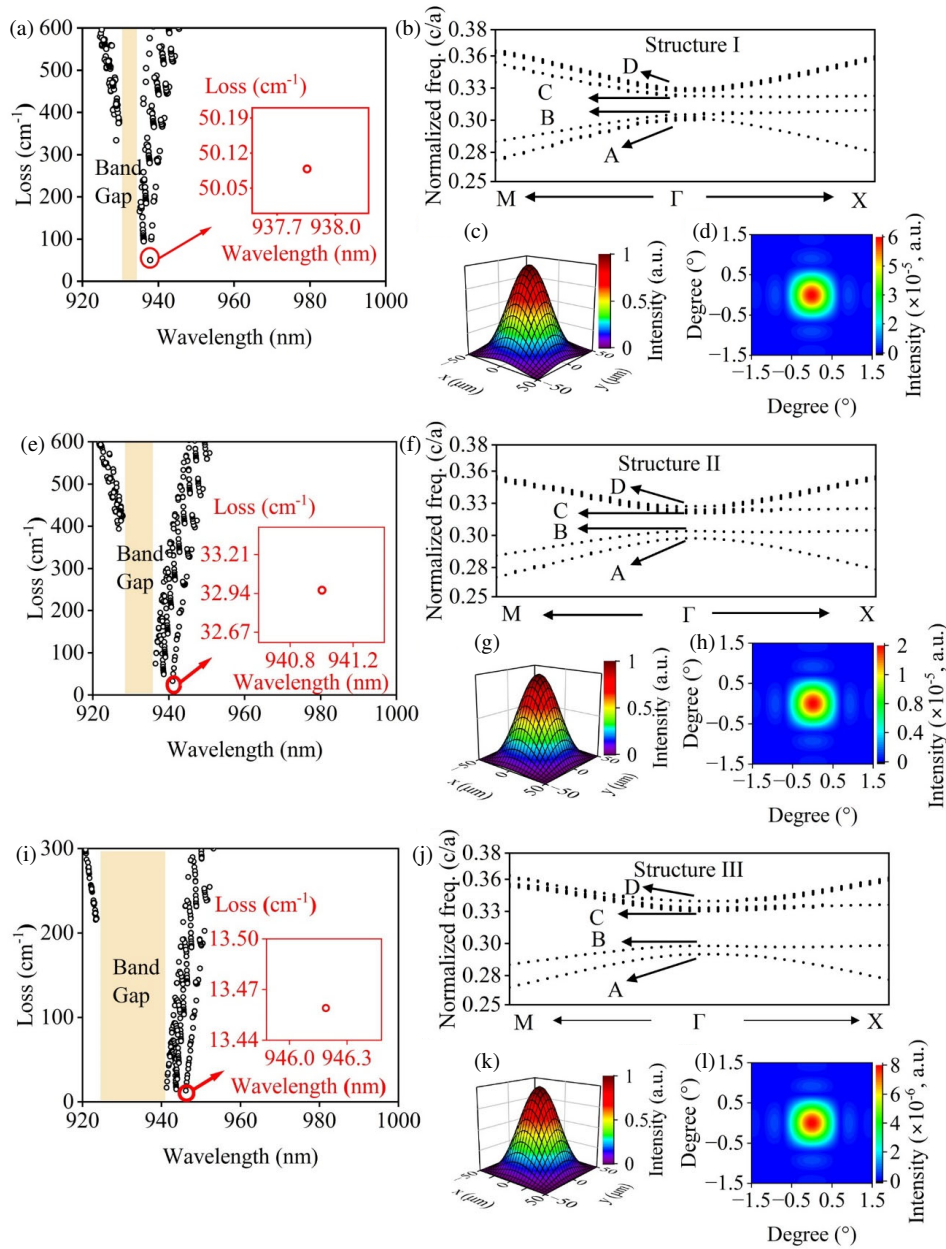
FIGURE 5. Relationship between loss and wavelength for structures (a) I, (e) II, and (i) III. The calculated band diagrams for structures (b) I, (f) II, and (j) III are presented, with modes A, B, C, and D identified. Calculated field intensity for structures (c) I, (g) II, and (k) III. Calculated far-field pattern of lasing mode for structures (d) I, (h) II, and (l) III. These results show single lobes rather than the multiple lobes associated with higher-order modes.

TABLE 3. Relaxation oscillation frequencies of different structures with the current of 6 A.

Area	Relaxation Oscillation Frequency (GHz)		
	I	II	III
100 μm × 100 μm	26.31	27.97	14.65
300 μm × 300 μm	13.57	11.40	10.79

4. HIGH-SPEED PERFORMANCE ANALYSIS

4.1. Numerical Results Based on Time-Dependent 3D-CWT

The values of the parameters used for the following time-dependent simulation are shown in Table 1. Figure 6 illustrates the temporal evolution of carriers of the 100 μm × 100 μm and 300 μm × 300 μm size PCSELs with structures I, II, and III for the same current of 6 A. The current densities of the 100 μm × 100 μm and 300 μm × 300 μm size PCSELs are 6.7×10^8 A/m^2 and 1.0×10^8 A/m^2, respectively. The relaxation oscillation frequencies which are obtained from Figure 6 are listed in Table 3. The relaxation oscillation frequencies
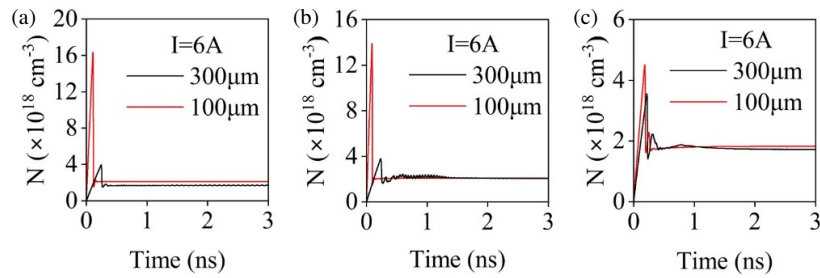
FIGURE 6. At current of 6 A, the temporal evolution of carriers indicates that the response rate of a 100 μm × 100 μm device is faster than that of a 300 μm × 300 μm device. The carrier density changes of 300 μm × 300 μm are plotted as the black line and 100 μm × 100 μm is plotted as the red line at the same current but different current densities. (a) is for structure I, (b) is for structure II, and (c) is for structure III.
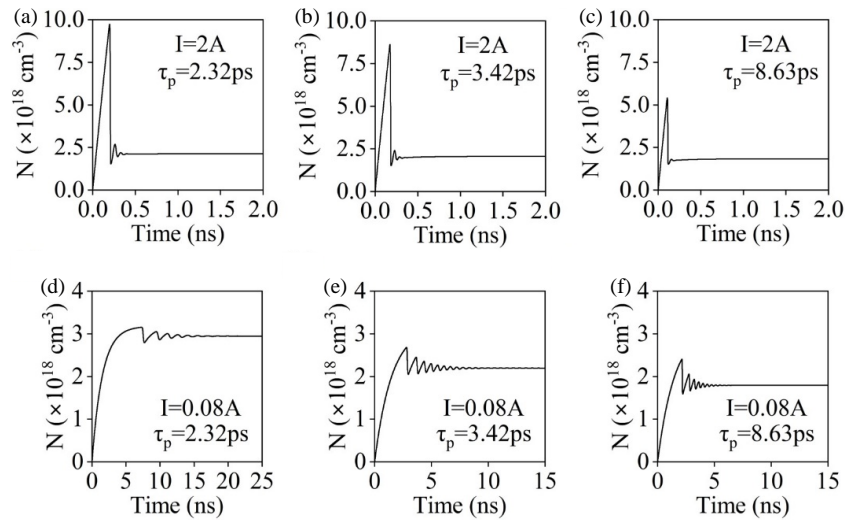

FIGURE 7. Carrier density temporal changes of three structures with the current (a)–(c) far above the threshold (2 A), and (d)–(f) close to threshold (0.08 A). (a) and (d) are for structure I, (b) and (e) are for structure II, and (c) and (f) are for structure III.

of the 100 μm × 100 μm devices are larger than those of the 300 μm × 300 μm devices. Larger relaxation oscillation frequency is beneficial to realizing a larger 3 dB modulation bandwidth; therefore, smaller-sized (100 × 100 μm) devices are considered in subsequent calculations.

The relaxation oscillation frequencies (f_r) can be estimated from Figure 7. At 2 A, f_r are 16 GHz, 17.38 GHz, and 18.94 GHz for structure I, structure II, and structure III, respectively. At 0.08 A, f_r are 0.47 GHz, 0.95 GHz, 1.46 GHz for structure I, structure II, and structure III, respectively.

Figure 7 and Figure 8 illustrate the temporal carrier density and power changes for three structures at different currents, including the current approaching the threshold (0.08 A) and the current above the threshold (2 A). The relaxation oscillation frequencies can be estimated from Figure 7. At 2 A, f_r are 16 GHz, 17.38 GHz, and 18.94 GHz for structure I, structure II, and structure III, respectively. At 0.08 A, f_r are 0.47 GHz, 0.95 GHz, 1.46 GHz for structure I, structure II, and structure III, respectively. When the D-factor is constant, the relaxation oscillation frequency is proportional to the current above the threshold, which is consistent with the results of the comparison. Moreover, structure III has the lowest relaxation frequency at 2 A, but at 6 A structure I has the lowest relaxation frequency

(obtained from Table 3). Simulations in the next section reveal that the lowest relaxation frequency corresponds to the lowest 3 dB bandwidth both at 2 A and 6 A. In addition, structure III has the highest damping estimated from Figure 7(c) at 2 A and takes the shortest time to be carrier-density-stable both at 0.08 A and 2 A. Larger damping brings faster flatting of the curve of frequency response under the large current of 4 A for structure III, which will be verified in the next section. In addition, it can be observed at 2 A from Figure 8 that the structure with a shorter photon lifetime exhibits higher power efficiency but lower high-speed frequency response. The device with higher power efficiency has larger amplitudes of optical signals, which is beneficial to the opening of eye diagrams under high-speed transmissions.

Figure 9 presents the photon density distribution after the power and carrier concentrations have stabilized, further confirming that all structures I, II, and III achieve stable lasing. At higher currents above the threshold, the photon density distribution covers a larger area, leading to some leakage in the carrier diffusion region outside the PC region. Edge loss increment weakens the confinement ability to optical fields of the photonic crystal resonator, resulting in leakage of optical fields.
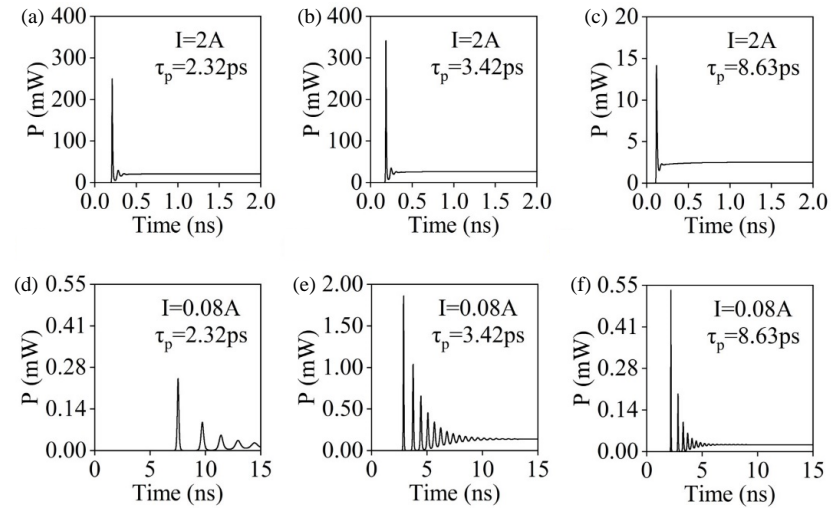
FIGURE 8. Power temporal changes of three structures with the current (a)–(c) far above the threshold, and (d)–(f) close to threshold (0.08 A). The stable power at 2 A is (a) 21 mW for structure I ($\tau_p = 2.32$ ps), (b) 26.7 mW for structure II ($\tau_p = 3.42$ ps), (c) 2.5 mW for structure III ($\tau_p = 8.63$ ps). The stable power at 0.08 A is ~ 0 W for (d) structure I ($\tau_p = 2.32$ ps), (e) structure II ($\tau_p = 3.42$ ps), and (f) structure III ($\tau_p = 8.63$ ps).
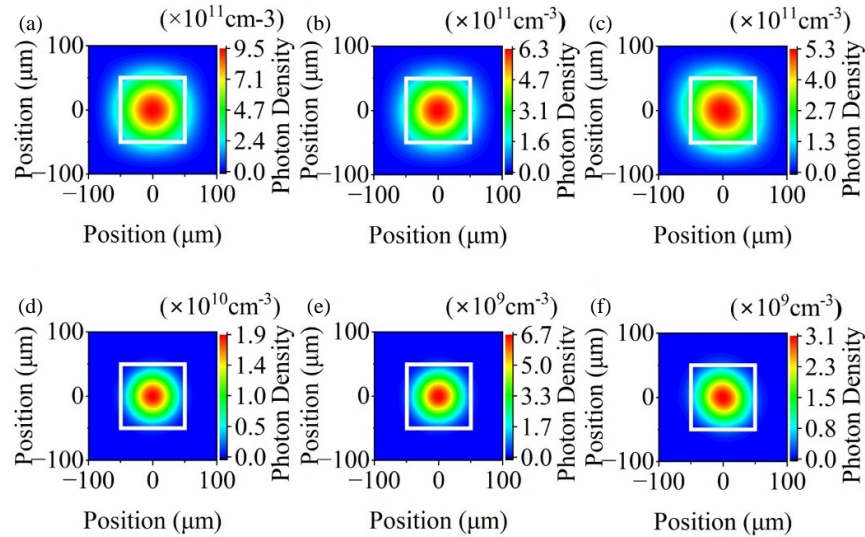

FIGURE 9. Photon density temporal changes of structure I at (a) 2 A and (d) 0.08 A, structure II at (b) 2 A and (e) 0.08 A, structure III at (c) 2 A and (f) 0.08 A.
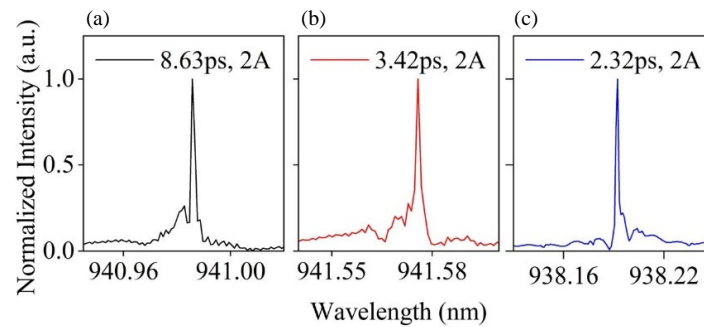

FIGURE 10. Simulated spectra for (a) structure I, (b) structure II, and (c) structure III.

Figure 10 shows the spectrum of three structures at 2 A. Spectrum is calculated by performing the Fourier analysis on the power-time curves. Here, single-mode lasing is achieved

with these three photonic-crystal laser structures, and the central wavelength of the main peak is around 940 nm with less than 2 nm difference from the designed wavelength for the three
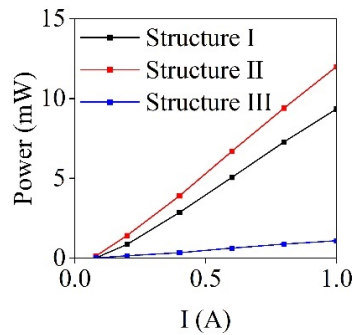
FIGURE 11. Simulated power characteristics for Structure I, II, and III. Threshold currents are approximately 0.08 A, 0.07 A, and 0.05 A.
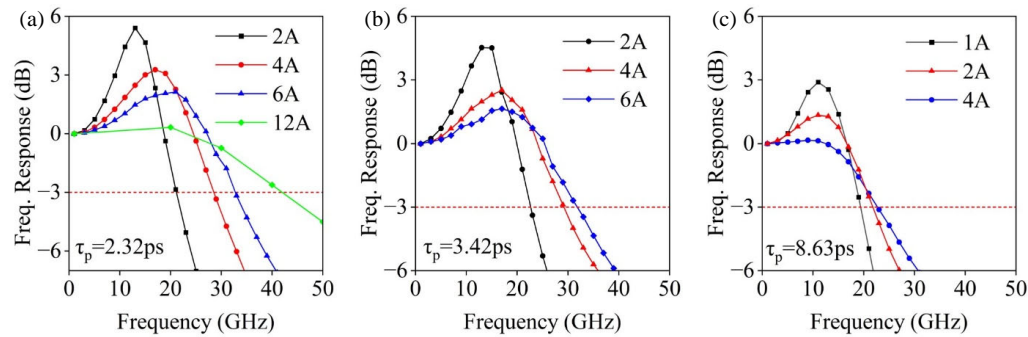

FIGURE 12. Small signal response of PCSELs with different photon lifetimes. (a) is for structure I ($\tau_p = 2.32$ ps) at 2 A, 4 A, 6 A and 12 A. The current of 12 A is for 3 dB bandwidth prediction at a large current. (b) is for structure II ($\tau_p = 3.42$ ps) at 2 A, 4 A and 6 A. (c) is for structure III ($\tau_p = 8.63$ ps) at 1 A, 2 A and 4 A. Since the curve of frequency response is flat at 4 A, the current is not necessary to increase to 6 A. Devices with larger currents and shorter photon lifetimes tend to exhibit larger bandwidth.

structures. Figure 11 illustrates the power-current relationships for three structures. Structures I and II show higher power efficiency, while structure III with the lowest threshold gain shows the lowest power efficiency. The threshold currents can be estimated by the curve, which are 0.08 A for I with the highest threshold gain, 0.07 A for II, and 0.05 A for III with the lowest threshold gain.

4.2. Small Signal Response and f₃ dB Bandwidth

In the calculation of time-dependent 3D-CWT for three structures, the small signal response is calculated by loading the small-amplitude sinusoid signal on the bias current above the threshold when the carrier density, photon density, and power are stable. Figure 12 shows the calculated small signal response values of the three PCSELs with the photon lifetime of 2.32 ps, 3.42 ps, and 8.63 ps under different bias currents. Based on the fitted curves, the $f_{3\,\text{dB}}$ bandwidths of structure I (2.32 ps) and structure II (3.42 ps) under 6 A bias current are 33 GHz and 31 GHz, respectively. Under a larger bias current before the thermal saturation, the $f_{3\,\text{dB}}$ bandwidth can be still larger.

The $f_{3\,\text{dB}}$ bandwidth increases as the photon lifetime and damping decreases, which is attributed to larger losses. This phenomenon can be observed in the figure of frequency response, where a shorter photon lifetime (2.32 ps) leads to a sharp peak at a lower current. Conversely, with a longer photon lifetime (8.63 ps), the associated losses are reduced, and the damping effect increases, requiring lower bias currents to

achieve a peak in the frequency response. In addition, the $f_{3\,\text{dB}}$ bandwidth of the device with a longer photon lifetime of 8.63 ps does not increase when the bias current increases from 2 A to 4 A, due to the dramatic decline of the frequency response caused by the suppression of high damping.

To verify accuracy of the calculation, the intrinsic frequency response of different photon lifetimes (2.32 ps, 3.42 ps, and 8.63 ps) at different currents above the threshold is calculated by the formula (7), and the 3 dB bandwidth is estimated. Results are shown in Figures 13(a), (b), and (c), which illustrate that lasers with smaller photon lifetime and larger injection current are capable of obtaining the largest 3 dB bandwidth. For $\tau_p = 2.32$ ps, the large current injection (12 A) is conducted, and more than 40 GHz 3 dB bandwidth is obtained when the curve approaches flatness.

There are limitations on the 3 dB bandwidth. Figure 12 shows that the $f_{3\,\text{dB}}$ bandwidth increases approximately linearly in the low-current region but exhibits saturation at large currents. This observation confirms that even without considering thermal effects, the $f_{3\,\text{dB}}$ bandwidth does not linearly increase without limit. Due to the rapid decline in the frequency response curve after the resonance peak, devices with longer photon lifetime and larger damping are more prone to bandwidth saturation as the current increases. The maximum $f_{3\,\text{dB}}$ bandwidth is calculated by [32]:

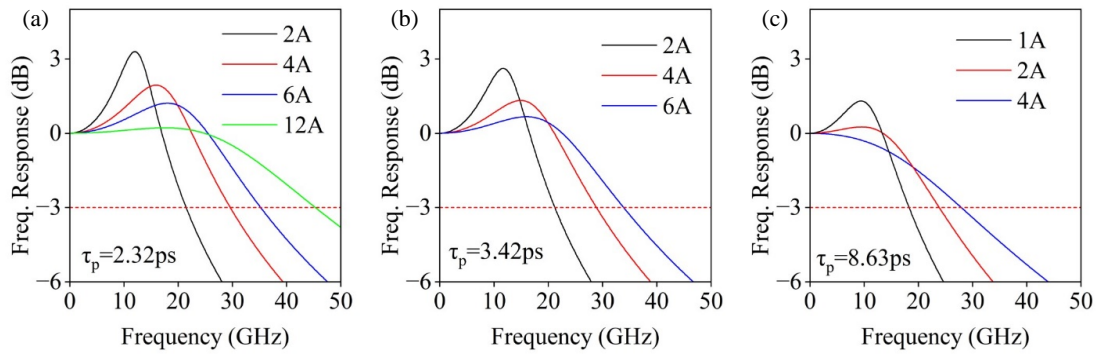$$f_{3\,\text{dB}} \approx \frac{2\sqrt{2}}{K}, \tag{10}$$

FIGURE 13. Intrinsic response of PCSELs with different photon lifetimes, calculated by Equation (7). (a) is for ($\tau_p = 2.32\,\mathrm{ps}$) at 2 A, 4 A, 6 A and 12 A. The current of 12 A is for the largest 3 dB bandwidth prediction. (b) is for ($\tau_p = 3.42\,\mathrm{ps}$) at 2 A, 4 A and 6 A. (c) is for ($\tau_p = 8.63\,\mathrm{ps}$) at 1 A, 2 A, and 4 A. Devices with larger currents and shorter photon lifetimes exhibit larger bandwidths.
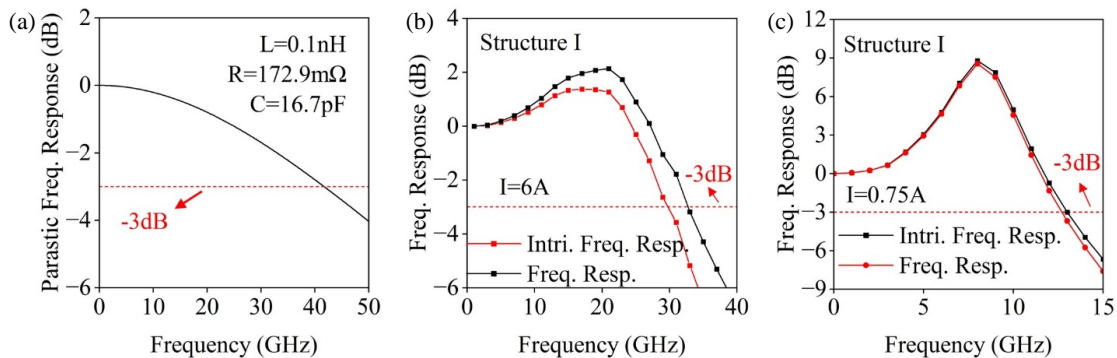

FIGURE 14. (a) Parasitic frequency response for $L = 0.1\,\mathrm{nH}$, $R = 172.9\,\mathrm{m\Omega}$ and $C = 16.7\,\mathrm{pF}$. (b) The total frequency response is 29 GHz for structure I at 6 A, which shows the largest intrinsic 3 dB bandwidth out of three structures at the injection current. (c) The intrinsic and total frequency response at 0.75 A. Structure I exhibits a slight reduction in the 3 dB bandwidth compared to the higher current of 6 A due to the pronounced parasitic effect at higher frequencies.

The predicted intrinsic $f_{3\,\mathrm{dB}}$ bandwidth of structure I is over 90 GHz, which is comparable to that of the VCSEL. However, it should be pointed out that thermal and parasitic effects will reduce the $f_{3\,\mathrm{dB}}$ bandwidth [18]. Figure 14(a) shows the result of the parasitic frequency response, which is based on the calculation of the parasitic frequency response as referenced in [18]. Figures 14(b) and (c) present the frequency response results, considering both intrinsic and parasitic effects, for structure I at large and small current, respectively. At current of 6 A, the 3 dB bandwidth is reduced to 29 GHz with parasitic effect. Parameters are wire inductance L (0.1 nH), series resistance R (172.9 mΩ), and capacitance C (16.7 pF), which are referenced to [18]. As illustrated in Figures 14(b) and 14(c), the $f_{3\,\mathrm{dB}}$ with parasitic effect at 6 A experiences larger reduction than that at 0.75 A. This is attributed to the stronger parasitic effect at larger frequency.

In the previous section, the power characteristics are analyzed. It indicates that at a given current the power decreases as loss increases. Given the focus on achieving high-speed modulation and the potential of long-distance transmission, the tradeoff between power and bandwidth is to be considered. A reasonable approach for it is photon lifetime tuning.

4.3. Large Signal Response

As shown in Figures 15(a) and (b), 60 Gb/s NRZ eye diagrams are simulated for PCSELs with the photon lifetimes of 2.32 ps and 3.42 ps under the same current. It is verified that the PCSEL with the photon lifetime of 2.32 ps exhibits better signal clarity and integrity than that of 3.42 ps. This is because the larger bandwidth device results in a faster rise time [38]. As shown in Figures 15(c) and (d), eye diagrams for the large-bandwidth PCSEL (photon lifetime of 2.32 ps) are simulated under different bias currents. By using a larger current, the quality of the eye diagram is improved with a smaller overshoot and larger opening. This is because the larger current leads to a larger $f_{3\,\mathrm{dB}}$ bandwidth resulting in a shorter relaxation oscillation time, and also the larger current leads to a larger damping effectively suppressing the overshoot. In Figure 15(e), the 100 Gb/s NRZ eye diagram under 8 A bias current is realized.

A larger damping is beneficial to a flat frequency response and reduces the overshoot at lower current levels. From formulas (8) and (9), by increasing K-factor and resonance frequency f_r, damping can be increased. A larger K-factor can be realized by a larger photon lifetime, which can be achieved by optimizing the lattice of the photonic crystal. A larger f_r can be real-
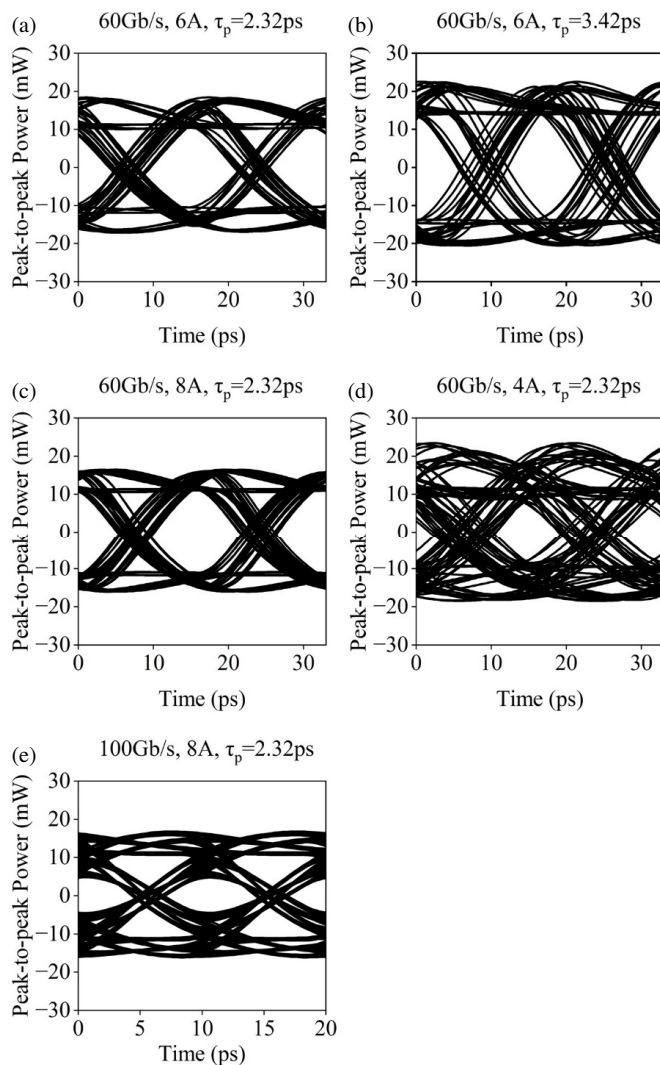
FIGURE 15. NRZ eye diagrams. (a) 60 Gb/s eye diagram of the PC-SELs with 2.32 ps photon lifetime under 6 A current, (b) 60 Gb/s eye diagram of the PCSELs with 3.42 ps photon lifetime under 6 A current, (c) 60 Gb/s eye diagram of the PCSELs with 2.32 ps photon lifetime under 8 A current, (d) 60 Gb/s eye diagram of the PCSELs with 2.32 ps photon lifetime under 4 A current, (e) 100 Gb/s eye diagram of the PC-SELs with 2.32 ps photon lifetime under 8 A current.

ized by a larger D-factor, which can be achieved by optimizing the epitaxial design to increase the optical confinement factor. However, the damping should be optimized, because too large damping will lead to a decrease of the 3 dB bandwidth.

5. CONCLUSIONS

We have performed the output power, modes, and small signal response of the PCSELs with double-lattice photonic crystals via the 3D-CWT method and introduced the design principle for the high-speed PCSELs. We show that the resonance frequency of the PCSELs can be increased by reducing the size of the PC-SELs, and the photon lifetime and the damping of the PCSELs can be decreased by optimizing the distance between the double lattice and the diameters of the double lattice. The large resonance frequency and small damping lead to over 40 GHz intrinsic 3 dB modulation bandwidth of the PCSELs and enable over

100 Gbit/s single-lane optical transmission under NRZ modulation. Our calculation is based on the classical PCSELs design; therefore, further enhancement of the 3 dB modulation bandwidth can be expected by

- optimizing the epitaxial design to increase the optical confinement factor,

- further decreasing the size of the PCSELs to decrease the volume,

- optimizing the lattice of the photonic crystal to decrease the photon lifetime, so as the damping,

- introducing the coplanar electrodes to decrease the capacitance.

We believe that the proposed device can be a promising candidate for high-speed, high-power, free-space optical communication.

ACKNOWLEDGEMENT

REFERENCES

[1] Yang, Y.-C., H.-T. Cheng, and C.-H. Wu, "Single-channel 106.25 Gb/s PAM-4 and 64 Gb/s NRZ transmission with a 33.4-GHz 850-nm VCSEL with low-RIN characteristics," *Journal of Lightwave Technology*, Vol. 42, No. 1, 293–301, 2024.

[2] Haghighi, N., G. Larisch, R. Rosales, M. Zorn, and J. A. Lott, "35 GHz bandwidth with directly current modulated 980 nm oxide aperture single cavity VCSELs," in *2018 IEEE International Semiconductor Laser Conference (ISLC)*, 1–2, Santa Fe, NM, USA, Sep. 2018.

[3] Ge, C., L. Dong, X. Gu, and F. Koyama, "1060 nm single-mode intra-cavity metal-aperture VCSEL for over 2 km standard 1300 nm SMF transmission," in *2023 Conference on Lasers and Electro-Optics (CLEO)*, 1–2, San Jose, CA, USA, 2023.

[4] Murty, M. V. R., J. Wang, S. Jiang, D. Dolfi, T. K. Wang, D. Vaughan, Z.-W. Feng, N. Leong, A. Sridhara, S. T. Joyo, J. Chu, and L. Giovane, "Toward 200 G per lane VCSEL-based multimode links," in *2024 Optical Fiber Communications Conference and Exhibition (OFC)*, San Diego, CA, USA, 2024.

[5] Shimizu, S., C. Ge, L. Dong, X. Gu, A. Matsumoto, S. Shinada, and F. Koyama, "Record high-baud-rate 128-Gbit/s NRZ-OOK direct modulation of 1060-nm single-mode VCSEL for transmission over 2-km standard SMF," in *2023 Opto-Electronics and Communications Conference (OECC)*, 1–4, Shanghai, China, 2023.

[6] Jiang, S., J. Wang, M. V. R. Murty, Z.-W. Feng, G.-H. Koh, S.-J. Taslim, A. Sridhara, X. Cai, N. Leong, D. W. Dolfi, J. Chu, and

L. M. Giovane, "Development and characterization of 100 Gb/s 940 nm VCSELs for multimode optical links," in *Vertical-Cavity Surface-Emitting Lasers XXVIII*, Vol. 1290406, 35–40, San Francisco, California, USA, 2024.

[7] Zuo, T., T. Zhang, S. Zhang, and L. Liu, "Single-lane 200-Gbps PAM-4 transmission for datacenter intra-connections employing 850-nm VCSEL," in *2020 Asia Communications and Photonics Conference (ACP) and International Conference on Information Photonics and Optical Communications (IPOC)*, Beijing, China, 2020.

[8] Inoue, T., T. Kim, S. Katsuno, R. Morita, M. Yoshida, M. D. Zoysa, K. Ishizaki, and S. Noda, "Measurement and numerical analysis of intrinsic spectral linewidths of photonic-crystal surface-emitting lasers," *Applied Physics Letters*, Vol. 122, No. 5, 051101, 2023.

[9] Hirose, K., Y. Liang, Y. Kurosaka, A. Watanabe, T. Sugiyama, and S. Noda, "Watt-class high-power, high-beam-quality photonic-crystal lasers," *Nature Photonics*, Vol. 8, No. 5, 406–411, 2014.

[10] Inoue, T., M. Yoshida, J. Gelleta, K. Izumi, K. Yoshida, K. Ishizaki, M. D. Zoysa, and S. Noda, "General recipe to realize photonic-crystal surface-emitting lasers with 100-W-to-1-kW single-mode operation," *Nature Communications*, Vol. 13, No. 1, 3262, 2022.

[11] Yoshida, M., S. Katsuno, T. Inoue, J. Gelleta, K. Izumi, M. D. Zoysa, K. Ishizaki, and S. Noda, "High-brightness scalable continuous-wave single-mode photonic-crystal laser," *Nature*, Vol. 618, No. 7966, 727–732, 2023.

[12] Itoh, Y., N. Kono, D. Inoue, N. Fujiwara, M. Ogasawara, K. Fujii, H. Yoshinaga, H. Yagi, M. Yanagisawa, M. Yoshida, *et al.*, "High-power CW oscillation of 1.3-μm wavelength InP-based photonic-crystal surface-emitting lasers," *Optics Express*, Vol. 30, No. 16, 29 539–29 545, 2022.

[13] Inoue, T., M. Yoshida, M. D. Zoysa, K. Ishizaki, and S. Noda, "Design of photonic-crystal surface-emitting lasers with enhanced in-plane optical feedback for high-speed operation," *Optics Express*, Vol. 28, No. 4, 5050–5057, 2020.

[14] Li, R., Y. Xu, S. Zhang, Y. Ma, J. Liu, B. Zhou, L. Wang, N. Zhuo, J. Liu, J. Zhang, *et al.*, "High brightness terahertz quantum cascade laser with near-diffraction-limited Gaussian beam," *Light: Science & Applications*, Vol. 13, No. 1, 193, 2024.

[15] Yoshida, M., M. D. Zoysa, K. Ishizaki, Y. Tanaka, M. Kawasaki, R. Hatsuda, B. Song, J. Gelleta, and S. Noda, "Double-lattice photonic-crystal resonators enabling high-brightness semiconductor lasers with symmetric narrow-divergence beams," *Nature Materials*, Vol. 18, No. 2, 121–128, 2019.

[16] Inoue, T., R. Morita, K. Nigo, M. Yoshida, M. D. Zoysa, K. Ishizaki, and S. Noda, "Self-evolving photonic crystals for ultrafast photonics," *Nature Communications*, Vol. 14, No. 1, 50, 2023.

[17] Ishimura, S., R. Morita, T. Inoue, K. Nishimura, H. Takahashi, T. Tsuritani, M. D. Zoysa, K. Ishizaki, M. Suzuki, and S. Noda, "Proposal and demonstration of free-space optical communication using photonic crystal surface-emitting lasers," *Journal of Lightwave Technology*, Vol. 41, No. 12, 3688–3694, 2023.

[18] Morita, R., S. Ishimura, T. Inoue, K. Nishimura, H. Takahashi, T. Tsuritani, M. D. Zoysa, K. Ishizaki, M. Suzuki, and S. Noda, "High-speed high-power free-space optical communication via directly modulated watt-class photonic-crystal surface-emitting lasers," *Optica*, Vol. 11, No. 7, 971–979, 2024.

[19] Chan, V. W. S., "Optical satellite networks," *Journal of Lightwave Technology*, Vol. 21, No. 11, 2811, 2003.

[20] Peng, C.-Y., H.-T. Cheng, Y.-H. Hong, W.-C. Hsu, F.-H. Hsiao, T.-C. Lu, S.-W. Chang, S.-C. Chen, C.-H. Wu, and H.-C. Kuo, "Performance analyses of photonic-crystal surface-emitting laser: Toward high-speed optical communication," *Nanoscale Research Letters*, Vol. 17, No. 1, 90, 2022.

[21] Pan, M., C. Gautam, A. Kalapala, Y. Chen, T. Rotter, M. Zhou, R. Gibson, R. Bedford, S. Fan, G. Balakrishnan, and W. Zhou, "Frequency response characteristics of high-power photonic crystal surface-emitting lasers," in *2023 IEEE Photonics Conference (IPC)*, 1–2, Orlando, Florida, USA, 2023.

[22] Orchard, J. R., P. Ivanov, A. F. McKenzie, C. H. Hill, I. Javed, C. W. Munro, J. Kettle, R. A. Hogg, D. T. D. Childs, and R. J. E. Taylor, "Small signal modulation of photonic crystal surface emitting lasers," *Scientific Reports*, Vol. 13, No. 1, 19019, 2023.

[23] Inoue, T., R. Morita, M. Yoshida, M. D. Zoysa, Y. Tanaka, and S. Noda, "Comprehensive analysis of photonic-crystal surface-emitting lasers via time-dependent three-dimensional coupled-wave theory," *Physical Review B*, Vol. 99, No. 3, 035308, 2019.

[24] Kalapala, A., A. Y. Song, M. Pan, C. Gautam, L. Overman, K. Reilly, T. J. Rotter, G. Balakrishnan, R. Gibson, R. Bedford, J. J. Coleman, S. Fan, and W. Zhou, "Scaling challenges in high power photonic crystal surface-emitting lasers," *IEEE Journal of Quantum Electronics*, Vol. 58, No. 4, 1–9, 2022.

[25] Zhou, M., A. R. K. Kalapala, M. Pan, R. Gibson, K. J. Reilly, T. Rotter, G. Balakrishnan, R. Bedford, W. Zhou, and S. Fan, "Increasing the Q-contrast in large photonic crystal slab resonators using bound-states-in-continuum," *ACS Photonics*, Vol. 10, No. 5, 1519–1528, 2023.

[26] Gelleta, J., Y. Liang, H. Kitagawa, and S. Noda, "Influence of external reflection on the TE mode of photonic crystal surface-emitting lasers," *Journal of the Optical Society of America B*, Vol. 32, No. 7, 1435–1441, 2015.

[27] Taylor, R. J. E., G. Li, P. Ivanov, D. T. D. Childs, T. S. Roberts, B. J. Stevens, B. Harrison, J. Sarma, N. Babazadeh, G. Terrnent, and R. A. Hogg, "Mode control in photonic crystal surface emitting lasers through external reflection," *IEEE Journal of Selected Topics in Quantum Electronics*, Vol. 23, No. 6, 1–8, 2017.

[28] Bian, Z., X. Zhao, K. J. Rae, A. S. M. Kyaw, D. Kim, A. F. McKenzie, B. C. King, J. Liu, S. Thoms, P. Reynolds, *et al.*, "Resonator embedded photonic crystal surface emitting lasers," in *2022 28th International Semiconductor Laser Conference (ISLC)*, 1–2, Matsue, Japan, 2022.

[29] Sakai, K., E. Miyai, and S. Noda, "Coupled-wave theory for square-lattice photonic crystal lasers with TE polarization," *IEEE Journal of Quantum Electronics*, Vol. 46, No. 5, 788–795, 2010.

[30] Liang, Y., C. Peng, K. Sakai, S. Iwahashi, and S. Noda, "Three-dimensional coupled-wave analysis for square-lattice photonic crystal surface emitting lasers with transverse-electric polarization: Finite-size effects," *Optics Express*, Vol. 20, No. 14, 15 945–15 961, 2012.

[31] Otsuka, K., K. Sakai, Y. Kurosaka, J. Kashiwagi, W. Kunishi, D. Ohnishi, and S. Noda, "High-power surface-emitting photonic crystal laser," in *LEOS 2007 — IEEE Lasers and Electro-Optics Society Annual Meeting Conference Proceedings*, 562–563, Lake Buena Vista, FL, USA, 2007.

[32] Coldren, L. A., S. W. Corzine, and M. L. Mashanovitch, *Diode Lasers and Photonic Integrated Circuits*, John Wiley & Sons, Hoboken, N.J., 2012.

[33] Tian, S.-C., M. Ahamed, G. Larisch, and D. Bimberg, "Novel energy-efficient designs of vertical-cavity surface emitting lasers for the next generations of photonic systems," *Japanese Journal of Applied Physics*, Vol. 61, No. SK, SK0801, 2022.

[34] Tian, S.-C., M. Ahamed, and D. Bimberg, "Progress in short wavelength energy-efficient high-speed vertical-cavity surface-emitting lasers for data communication," in *Photonics*, Vol. 10, No. 4, 410, 2023.

[35] Westbergh, P., J. S. Gustavsson, B. Kögel, A. Haglund, and A. Larsson, "Impact of photon lifetime on high-speed VCSEL performance," *IEEE Journal of Selected Topics in Quantum Electronics*, Vol. 17, No. 6, 1603–1613, 2011.

[36] Larisch, G., P. Moser, J. A. Lott, and D. Bimberg, "Impact of photon lifetime on the temperature stability of 50 Gb/s 980 nm VCSELs," *IEEE Photonics Technology Letters*, Vol. 28, No. 21, 2327–2330, 2016.

[37] Larisch, G., S. Tian, and D. Bimberg, "Optimization of VCSEL photon lifetime for minimum energy consumption at varying bit rates," *Optics Express*, Vol. 28, No. 13, 18 931–18 937, 2020.

[38] Haglund, E. P., P. Westbergh, J. S. Gustavsson, and A. Larsson, "Impact of damping on high-speed large signal VCSEL dynamics," *Journal of Lightwave Technology*, Vol. 33, No. 4, 795–801, 2014.